High spatial frequency laser induced periodic surface structure formation in germanium by mid-IR femtosecond pulses

Drake. R. Austin,[1,a)] Kyle R. P. Kafka,[1] Yu Hang Lai,[1] Zhou Wang,[1] Kaikai Zhang,[1] Hui Li,[2] Cosmin I. Blaga,[1] Allen Y. Yi,[2] Louis F. DiMauro,[1] and Enam A. Chowdhury[1]
[1]*The Ohio State University, 191 West Woodruff Ave, Columbus, Ohio 43210, USA*
[2]*The Ohio State University, 1971 Neil Ave, Columbus, Ohio 43210, USA*

(Received 29 June 2016; accepted 29 September 2016; published online 12 October 2016)

Formation of high spatial frequency laser induced periodic surface structures (HSFL) in germanium by 90 fs mid-IR pulses at a 1 kHz repetition rate with wavelengths between $\lambda = 2$ and 3.6 μm was studied with varying angle of incidence and polarization. The period of these structures varied from $\lambda/3$ to $\lambda/8$. A modified surface-scattering model including Drude excitation and the optical Kerr effect explains the spatial period scaling of HSFL across the mid-IR wavelengths. Transmission electron microscopy shows the presence of a 30 nm amorphous layer above the structure of crystalline germanium. Various mechanisms including two photon absorption and defect-induced amorphization are discussed as probable causes for the formation of this layer. *Published by AIP Publishing*. [http://dx.doi.org/10.1063/1.4964737]

I. INTRODUCTION

Laser induced periodic surface structures (LIPSS) have been studied for decades[1] as a topic on surface science and engineering. This single step technique can produce highly ordered nano-scale features on virtually any surface from metals and semiconductors to insulators, opening the door to wide ranging applications.[2] Among semiconductors, the femtosecond laser processing may have applications in opto-electronics,[3] solar cells,[4] etc. Germanium has been gaining attention steadily due to its much wider transparency band from $\lambda = 2$–17 μm, exceptionally high hole mobility,[5] and high third order non-linearity (greater than that of silicon by almost an order of magnitude). Nano-[6] and micro-structure formation in Ge[7] is of particular interest at longer wavelengths for waveguides,[8] molecular sensors,[9] and integrated photonic,[10,11] plasmonic devices,[12] and high-efficiency solar cells.[13] Although there is a tremendous interest in mid- and far-IR light-matter interaction at present,[14–16] femtosecond LIPSS work beyond 2 μm wavelengths is almost non-existent. Ultrashort pulses interacting with solids at mid-IR or longer wavelengths present an interesting paradigm, for several reasons, some of which are described as follows: (1) Many traditional semiconductors in this regime are transparent and behave like a dielectric. (2) Valence to conduction band transition mechanisms, especially for wide bandgap materials, would change from multiphoton to tunneling ionization in this regime. (3) As electron cycle average energy scales as λ^2, short pulse mid-IR laser excited electrons at modest intensities may gain enough energy to modify short pulse solid damage/ablation mechanism at long wavelengths.

We report here a systematic study of the formation of high spatial frequency laser induced periodic surface structures (HSFL) in Ge using sub-bandgap intense photon fields at wavelengths between 2 and 3.6 μm at 0, 45, and 76° angles of incidence. Similar types of HSFL formation have been reported in high bandgap materials (diamond) with laser pulses having photon energies far below the bandgap,[17] where an unmodified Sipe model was used to explain the HSFL period and orientation. In this model, the incident laser light interferes with a surface-scattered wave produced during the irradiation of a rough surface, leading to spatially periodic energy absorption on the surface.[18] Previous attempts by others to produce HSFL on Ge either did not succeed[19] or required chemical etching of the surface to reveal highly disordered "HSFL" formations perpendicular to the near-IR laser polarization,[20] where an induced $\chi^{(2)}$ coupling was suggested as a generation mechanism.[19] Low spatial frequency LIPSS (LSFL, with period $\Lambda \geq \lambda/2$) were studied previously on Ge,[21] but were formed at higher fluences by the excitation of surface plasmon polaritons (SPPs) and their subsequent interference with the incident laser light.[22] In this article, we present a distinct mid-IR HSFL formation mechanism based on a Sipe-Drude-Kerr (SDK) surface scattering model that takes into account electron excitation and the optical Kerr effect, resulting in excellent agreement with experimental observations.

II. EXPERIMENTAL METHODS

The experimental setup is similar to that described in detail by Austin *et al.*[21] Two optical parametric amplifier (OPA) systems were used in this experiment to generate the range of wavelengths at a 1 kHz repetition rate: (1) A HE-Topas-Prime (Light Conversion) pumped by a homebuilt Ti:Sapphire system to generate 2–2.4 μm wavelength, 100 fs pulses and (2) a homebuilt OPA to generate 3–3.6 μm wavelength, 90 fs pulses, which was also used in the LSFL generation studies.[21] These pulses were focused onto the sample using a 100 mm focal length, plano-convex CaF_2 lens mounted on a three-axis translation stage system with the tip-tilt adjustment. The focal spot at each wavelength was carefully characterized using an imaging system with a mid-IR camera (Dataray, WincamD). The resulting focal spot waist radii in the surface plane were 25, 34, and 35 μm

a)Electronic mail: austin.280@osu.edu

for 2.0, 2.4, and 3.6 μm wavelengths, respectively, and 49×22 μm for the 3.0 μm wavelength beam. The studied damage spots were formed with peak fluences from 0.35 to 0.38 J/cm^2, high enough to induce the formation of HSFL, but not LSFL (throughout this paper, all fluences are reported as their beam-normal value). The absolute pulse number interacting with a fresh Ge site was monitored by a triggered PbSe photodiode (Thorlabs PDA20H) and the speed of the triggered mechanical shutter limited the lowest number of pulses that could be selected consistently to 7 pulses. The multi-shot ablation threshold for Ge at $\lambda = 3.6$ μm (p-polarized) was also evaluated by varying the fluence until the probability of ablation crater formation reached 0%. The 7-pulse ablation threshold was measured to be 0.41 J/cm^2. The laser pulse fluences for the experimental results reported here were therefore kept below the single-pulse ablation threshold as it is widely known in the field of laser damage that ablation threshold decreases with pulse number.[24]

The 1 cm^2 single crystal and $\langle 100 \rangle$ n-type undoped Ge samples with resistivity $\sim$30 Ω cm were obtained from MTI Corporation. Post analysis of the damage spots was performed using SEM (FEI, Helios Nanolab 600 Dual Beam), transmission electron microscopy (TEM) (FEI/Philips, CM-200 T), atomic force microscopy (AFM) (Flex-Axiom, Nanosurf), and an interferometric depth profiler (IDP) (Veeco, Wyko NT9100).

III. RESULTS

A. Measured HSFL periods

The HSFL period versus wavelength was recorded at $\lambda = 2$, 2.4, 3, and 3.6 μm wavelengths under $\theta = 45°$ illumination (p-polarized for all wavelengths, both s- and p-polarized for 3 and 3.6 μm wavelengths), whereas the angular dependence was obtained at 0, 45, and 76° at $\lambda = 2.4$ μm. For reference, Brewster's angle for Ge at mid-IR wavelengths is 76°. HSFL were observed to form both in the central region of the damage spot as well as in the periphery (Fig. 1(b)), though never in the intermediate region. HSFL were oriented parallel to the laser polarization, ruling out second harmonic generation as a probable cause.[20,25] The central HSFL periods were determined by taking the 2D Fourier transform of SEM and IDP images and identifying peaks in the spectra, whereas the peripheral HSFL periods were determined by taking multiple lineouts. The experimental results are presented in Fig. 2, showing the measured period Λ (normalized to the laser wavelength) as a function of wavelength for 100 p-polarized pulses, revealing an approximately linear dependence and no noticeable dependence on θ. The central and peripheral HSFL are represented by filled and unfilled markers, respectively. The periods of peripheral HSFL decreased with increasing distance from the center, possibly due to the decrease in local fluence. In Fig. 2, the shortest consistently observed periods of the peripheral HSFL are presented for simplicity; they were found to be approximately half the period of the central HSFL. Example central HSFL images are also shown in Figs. 3(a)–3(d), comparing s- and p-polarizations at 3 and 3.6 μm wavelengths. In all cases, the orientation of the central HSFL remains parallel to the polarization. Despite the strong polarization dependence on Λ in the case of LSFL,[21] no significant variation with polarization is observed here with central HSFL.

B. Surface morphology

A cross-sectional specimen of the laser spot shown in Fig. 1(b) was prepared using a focused ion beam[26] (FEI Nova NanoLab 600 Dual Beam). An *in-situ* transfer was performed by attaching the specimen to a micromanipulator through platinum deposition. A final cut was then made, separating the specimen from the sample. After attaching the specimen to the TEM grid through additional platinum deposition, a final thinning was performed until reasonable electron transparency was achieved. Additionally, because the ion-assisted platinum layer deposition can result in the amorphization of the surface down to approximately 30 nm,[26] a thin ($\sim$40 nm) layer of gold was first deposited onto the sample using 1 kV DC sputtering, protecting the surface of the Ge from the

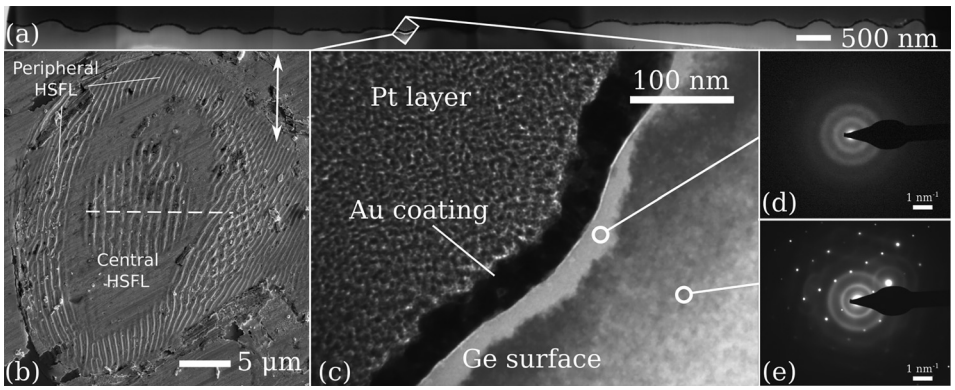

FIG. 1. (a) TEM cross section showing the structure of central HSFL on Ge ($\lambda = 2.4$ μm, $\theta = 0°$, 100 pulses, 0.36 J/cm^2). (b) SEM image of the (gold coated) damage spot chosen for the cross-section TEM imaging (arrow indicates polarization direction). The measured focal spot profile had a single maximum about the near-symmetric Gaussian profile; no increase in intensity was present to explain the reappearance of HSFL beyond the intermediate region. (c) High magnification TEM image of the Ge surface. Beneath the gold coating (black) is an oxide layer $\sim$3 nm thick (consistent with that observed by Bonse *et al.*[23]), followed by an amorphous top layer of Ge capping bulk crystalline Ge. This amorphous layer is present throughout the cross-section. (d) Diffraction pattern of electrons transmitting through the brighter amorphous layer, showing no crystallinity. (e) Same as (d) but through the crystalline bulk, confirming the crystallinity. [See supplementary material for more details in (a)].

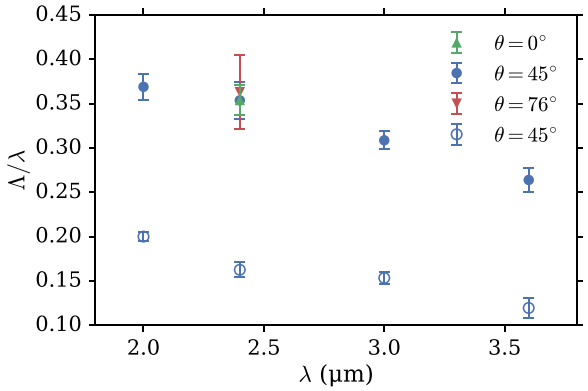

FIG. 2. HSFL period Λ (normalized to the laser wavelength λ) as a function of λ. The HSFL were produced using 100 pulses of p-polarized light. Sipe's model of HSFL formation would predict a constant Λ/λ across wavelengths; the observed deviations are consistent with the model which considers modification of the refractive index of Ge after laser-excitation. Also plotted are the shortest consistently observed periods of the peripheral HSFL (unfilled circles).

deposition process. Otherwise, any modifications to the surface observed under TEM, especially the formation of an amorphous layer, would not readily be attributed to laser exposure. Fig. 1 shows the selected TEM images of Ge HSFL formed at the center of the damage spot ($\lambda = 2.4\,\mu$m, $\theta = 0°$, 100 pulses). The electron energy was 200 keV and the camera length was 360 mm. The observed period at this wavelength was 850 ± 50 nm with a peak-to-trough height of 115 ± 25 nm. The AFM images (Fig. 3(e)) show similar surface morphology at 3.6 μm with shallower ripples further away from the center of the damage spot. Capping the surface of the crystalline Ge is an amorphous layer ~30 nm thick, similar to the depths reported in GaP, InP, Si, and SiC.[27–31] The formation of these layers has been attributed to the melting and subsequent rapid resolidification of the surface into a highly disordered structure after laser exposure.[28]

IV. DISCUSSION

As the observed central HSFL are always parallel to the polarization and exhibit periods $\sim\lambda/n$ (n is the refractive index of Ge), their origin can most likely be explained by the interference of the incident laser light with surface-scattered waves propagating within the transparent Ge. Similar LIPSS were observed by Höhm *et al.*[32,33] on fused silica using $\lambda = 800$ nm light. In the case of Ge with mid-IR light, however, the refractive index is significantly larger ($n \approx 4$), resulting in LIPSS with periods $\Lambda < \lambda/2$. While Young *et al.*[34] also studied LIPSS formation on Ge, nanosecond pulses with $\lambda = 1.06\,\mu$m (non-transparent regime) were used. For mid-IR pulses in the femtosecond regime, non-linear effects as well as the effects of electron excitation across the bandgap must be considered.

A. Description of theoretical model

HSFL formation was modeled using the theory of Sipe *et al.*[18] in which the interference of the incident laser pulse with a surface scattered wave (SSW) results in the inhomogeneous absorption of energy. As the initial light pulses impinge on the surface, they produce rough features off of which subsequent pulses may scatter. These surface scattered waves can propagate parallel to the surface and, in the case of transparent media, within the medium. These two waves will interfere with each other, causing spatially periodic energy absorption with wavevector $\mathbf{G}$ given by

$$\mathbf{G} = \mathbf{k}_s - \mathbf{k}_{\parallel}, \quad |\mathbf{G}| = 2\pi/\Lambda, \tag{1}$$

where $\mathbf{k}_{\parallel} = 2\pi \sin\theta/\lambda$ is the in-plane component of the incident light wavevector and $\mathbf{k}_s = 2\pi n/\lambda$ is the wavevector of the scattered wave (n is the refractive index of the medium). It is this inhomogeneous energy absorption that leads to spatially periodic damage patterns and, consequently, the formation of LIPSS with grating wavevector $\mathbf{G}$.

In general, these waves can scatter such that $\mathbf{k}_s$ points at arbitrary angles ϕ relative to $\mathbf{k}_{\parallel}$ (see Fig. 4 where p-polarization is horizontal and s-polarization is vertical), producing a wide range of possible grating wavevectors. However, the scattered waves will be produced at each angle with varying efficacy; the efficacy at which a given grating wavevector will be produced is given by the function $\eta(\mathbf{k}_{\parallel}, \mathbf{G})$. Bonse *et al.*[35] derived a series of equations that can be used to calculate this efficacy factor given the laser wavelength, polarization, angle of incidence, material permittivity, and the surface shape and filling factors that describe the surface roughness. Here, the shape and filling factors were chosen to be 0.4 and 0.7, respectively, as these were the values for Ge that best matched the original data reported by Young *et al.*[34]

Due to the preferential scattering of the incident light at particular angles, $\eta(\mathbf{G})$ exhibits peaks at the corresponding grating wavevectors (see, e.g., Fig. 5). In other words, the peaks correspond to the grating wavevectors that are most efficiently produced. With each additional pulse, these peaks

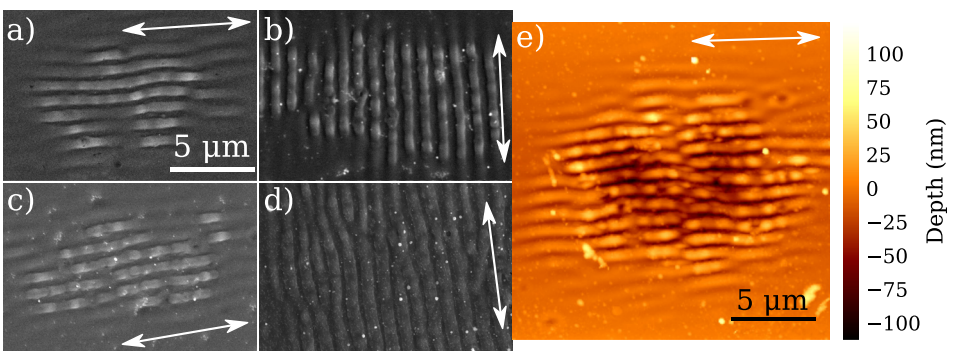

FIG. 3. (a)–(d) Example SEM images of central HSFL comparing p- and s-polarization HSFL at $\lambda = 3.6\,\mu$m (a, b, respectively) and $\lambda = 3.0\,\mu$m (c, d, respectively). All damage spots were formed using 100 pulses at $\theta = 45°$. The orientation of the HSFL is found to remain parallel to the polarization (arrows). No significant difference in period is observed. (e) AFM image of central HSFL on Ge showing the surface morphology (same laser conditions as in (a)).

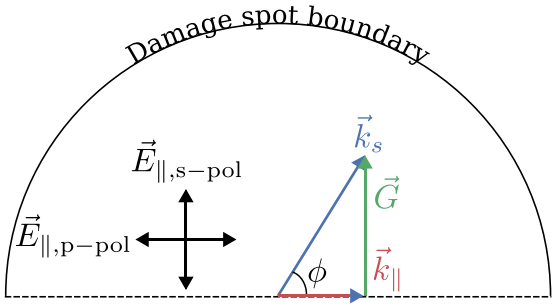

FIG. 4. Schematic diagram showing the top half of a circular damage spot (top view), demonstrating the key concepts of LIPSS formation from SSWs. Depicted are the wavevectors of the in-plane component of the incident light $\mathbf{k}_{\parallel}$, the SSW $\mathbf{k}_s$, and the grating wavevector $\mathbf{G}$ that results from the interference of the former two. The scattering angle ϕ describes the propagation direction of the SSW. In this coordinate system, any oblique incident light is taken to be incident from the left, in which case the in-plane component of the optical electric field $\mathbf{E}_{\parallel}$ is vertical for *s*-polarized light and horizontal for *p*-polarized light.

are reinforced through a feedback process in which the surface roughness develops Fourier components at these peaks, leading to increased efficiency for their production.

An analytical expression for the produced LIPSS period can also be found by considering the direction at which the incident light is more likely to scatter for a given polarization. For light incident on a hemispherical feature, the reflectivity (and, therefore, scattering) will be the greatest off of regions where the local polarization has the greatest *s*-component. This is simply a consequence of Fresnel reflection. Any *p*-components will experience greater transmission and refract into the bulk of the medium. For incident *s*-polarized light, the local polarization will be entirely *s* for reflecting planes corresponding to scatter in the $\phi = 0, \pi$ directions (perpendicular to the polarization). All other planes will have some component of *p*-polarization. For $\phi = 0, \pi$, Eq. (1) becomes

$$\frac{1}{\Lambda_s} = \frac{\sin\theta}{\lambda} - \frac{n}{\lambda}. \tag{2}$$

For the case of incident *p*-polarized light, the local polarization will be entirely *p* for reflecting planes corresponding to scatter in the $\phi = 0, \pi$ directions, resulting in the least scattering. The exact angles that led to maximum scattering result from incident light glancing off the sides of the hemispherical feature and gaining a transverse component of $\mathbf{k}_s$. Specifically, they are given by $\cos\phi = \frac{\sin\theta}{n}$. In this case, the expression for the LIPSS period can be determined from

$$\frac{1}{\Lambda_p^2} = \frac{n^2}{\lambda^2} - \frac{\sin^2\theta}{\lambda^2}. \tag{3}$$

Solving Eqs. (2) and (3) yields expressions for the LIPSS period for both *s*- and *p*-polarized light[36]

$$\Lambda_s = \frac{\lambda}{n - \sin\theta}, \quad \Lambda_p = \frac{\lambda}{\sqrt{n^2 - \sin^2\theta}}. \tag{4}$$

In both cases, the direction of $\mathbf{G}$ is perpendicular to the polarization so that the LIPSS themselves are parallel to it.

It is worth noting that, as stated by Sipe *et al.*, this theory does not offer a direct connection between the inhomogeneous energy absorption and the onset of material flow. However, as can be seen in the AFM results in Fig. 3, there is a net loss of material, suggesting that ablation has occurred. While the dynamics of LIPSS formation is still an active area of research, pump-probe experiments performed on Si by Murphy *et al.*[37] suggest that, after melting, the molten material experiences rapid expansion and removal with spatially periodic variations due to the inhomogeneous energy absorption. It is therefore reasonable to suggest that regions of greater energy absorption experience greater removal, resulting in valleys. Conversely, regions of lower energy absorption may experience expansion, but not lift-off of material, resulting in the hills located above the original surface height.

Because the LIPSS periods predicted by this model have a strong dependence on the refractive index, it is necessary to account for non-linear effects and ionization. This was achieved by treating the complex material permittivity as a combination of the non-excited value for Ge at the specified wavelength ($\epsilon_c \approx 16$ for mid-IR wavelengths),

$$\epsilon = \epsilon_c + \epsilon_{Drude} + \epsilon_{Kerr}, \tag{5}$$

together with modifications due to the Kerr effect as well as laser excitation according to the Drude model[25]

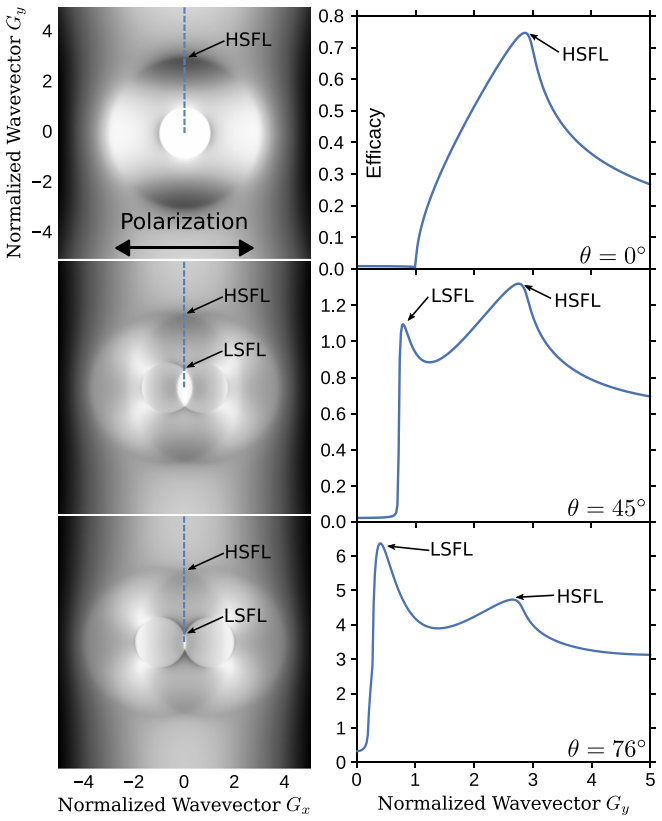

FIG. 5. Left: Plots of the efficacy factor $\eta(\mathbf{G})$ at $\lambda = 2.4\,\mu$m, $\theta = 0$, 45, and 76° with $n_e = 2.41 \times 10^{20}\,\mathrm{cm}^{-3}$. The polarization direction is indicated in the first image. Right: Vertical lineouts through the center. Peaks in this spectrum correspond to surface wave vectors that exhibit strong absorption and can therefore lead to LIPSS formation with orientation parallel to the laser polarization. A strong peak near the observed HSFL period is present, showing negligible variation with θ as observed experimentally. The peak is, however, observed to weaken at 76°, explaining the greater uncertainty in the period at that angle.

$$\epsilon_{Drude} = -\frac{\omega_p^2}{\omega(\omega + i\Gamma)}, \quad \epsilon_{Kerr} = \frac{3\chi^{(3)}I}{2n_0 c\epsilon_0} = 2n_0 n_2 I. \quad (6)$$

Here, $\omega_p = \sqrt{e^2 n_e / m^* \epsilon_0}$ is the plasma frequency, n_e is the conduction band electron density, m^* is the optical effective mass, and Γ is the electron collision frequency. The electron density was used as a free parameter corresponding to varying amounts of laser-excitation while values used for the optical effective mass and electron collision frequency were $m^* = 0.081\, m_e$ and $1/\Gamma = 46$ fs, respectively. The latter value was taken from Austin *et al.*[21] and corrected for the Kerr effect, which was not considered in that paper. It should be noted that the expression for ϵ_{Kerr} in Eq. (6) does not assume $\epsilon_{Kerr} \ll n_0^2$ as was done by Dufft *et al.*[25] The third-order susceptibility $\chi^{(3)}$ of Ge at each wavelength (and, consequently, the Kerr coefficient n_2) was taken from the theoretical dispersive curve presented by Hon *et al.*[38] that provided the best fit to the experimental data at mid-IR wavelengths. The Kerr effect cannot be neglected here for Ge as the values of n_2 are particularly high (0.38, 2.51, 2.07, and 1.46×10^{-13} cm^2/W for 2.0, 2.4, 3.0, and 3.6 μm wavelengths, respectively), significantly influencing HSFL formation.

B. Central HSFL

1. Angular and polarization dependence

The efficacy factor was calculated for each wavelength, polarization, and angle of incidence with varying electron density. An example plot of the efficacy factor for the 2.4 μm wavelength, *p*-polarized light at $\theta = 0$, 45, and 76° is shown in Fig. 5 with an electron density of 2.41×10^{20} cm^{-3}. The surface wave vector has been normalized to the laser wavelength. Multiple peaks are apparent, some with large periods corresponding to LSFL (not observed) and a peak at the observed HSFL period with an orientation parallel to the laser polarization (see vertical lineouts in Fig. 5). The location of this HSFL peak shows little variation with the angle of incidence and polarization, as observed experimentally (Figs. 2 and 3, respectively). However, this is inconsistent with the model of LIPSS formation in which SPPs are excited on the metallized surface and interfere with the incident laser light, which has been successfully used to explain observed properties of LSFL.[21,22] For *s*- and *p*-polarized light, the respective LIPSS periods predicted by this SPP model are given by

$$\Lambda_s = \frac{\lambda}{\sqrt{(\lambda/\lambda_s)^2 - \sin^2\theta}}, \quad \Lambda_p = \frac{\lambda}{\lambda/\lambda_s - \sin\theta}, \quad (7)$$

where λ_s is the SPP wavelength. However, the fact that typically $\lambda/\lambda_s \approx 1$ leads to a strong dependence on polarization and angle of incidence. It is therefore unlikely that the HSFL observed here are the result of SPP excitation. Additionally, the previously mentioned LSFL were only observed to form at higher fluences ($\gtrsim$0.4 J/cm^2), while HSFL were observed to form at lower fluences ($\lesssim$0.4 J/cm^2) and in the peripheries of damage spots. This is consistent with the requirement that $\mathrm{Re}[\epsilon] < -1$ in order for SPPs to form, a condition that is not satisfied until fluences high enough to cause sufficient ionization are achieved. Below this fluence, the surface remains non-metallic and the usual SSW-induced LIPSS dominate.

A similar analysis can be performed using Eq. (4). For the case of Ge at mid-IR wavelengths, $n \approx 4 \gg \sin\theta$ and $\Lambda_s \approx \Lambda_p \approx \lambda/n$, yielding little dependence on the polarization or angle of incidence, as observed. Additionally, a linear dependence of the spatial period on wavelength would be predicted for constant n, which was not observed in Fig. 2 due to deviations from linearity to the changes in n after laser excitation.

2. Electron density of central HSFL region

Efficacy plots similar to those in Fig. 5 were generated for each set of laser conditions, using the electron density as a fitting parameter. Fig. 6 summarizes this process by showing the variation of the efficacy factor with wavevector and electron density for the laser conditions that produced the central HSFL in Fig. 1. The peak of the efficacy factor is denoted by a white dashed line and is observed to shift to smaller wavevectors as the electron density increases. The black dotted line denotes the wavevector at which HSFL were observed to form; by tracing this line to the efficacy peak, a predicted value for the electron density can be extracted (green dotted line). This process was repeated at each wavelength for $\theta = 45°$ with *p*-polarization; the results are plotted in Fig. 7. The right axis is normalized to a surface critical density n_{crit} defined as the electron density at which the real part of Eq. (5) equates to zero, when the solid surface becomes metallic. In all cases, the observed HSFL wavevector could be matched using reasonable values of electron density (near critical density). When the Kerr effect is not included, the estimated electron densities decrease by a factor of 1.15 for $\lambda = 2.0\,\mu$m light (smallest $\chi^{(3)}$) and 1.94 for $\lambda = 2.4\,\mu$m light (largest $\chi^{(3)}$). In general, it appears that these central HSFL tend to form at $n_e \approx n_{crit}/2$. This is in contrast to the electron density found by Austin *et al.*[21] based on the LSFL analysis at 3.0 μm, which, after correcting for the Kerr

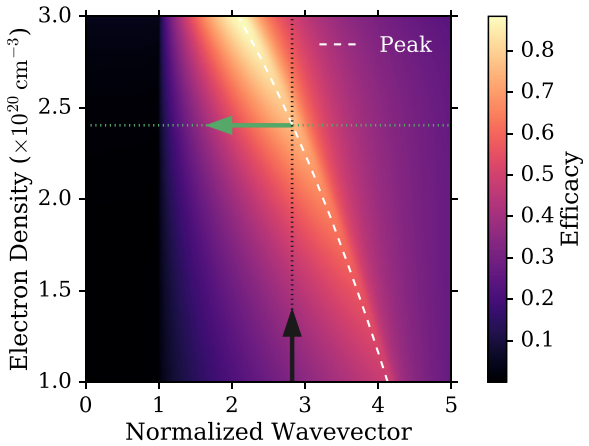

FIG. 6. Variation of efficacy factor with surface wavevector and electron density for $\lambda = 2.4\,\mu$m, $\theta = 0°$, 100 pulses. The white dashed curve traces out the peak of the efficacy for each electron density. The black dotted line corresponds to the observed HSFL period while the green dotted line corresponds to the electron density required for the efficacy peak to match this period.

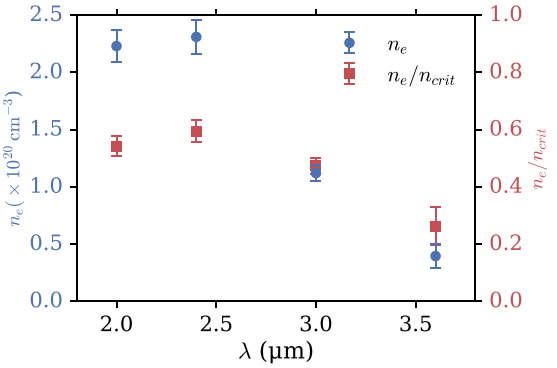

FIG. 7. Fitted electron density of the central HSFL region as a function of wavelength (100 pulses, $\theta = 45°$). The right axis has been scaled to a critical density defined as the electron density at which the real part of Eq. (5) equates to zero.

effect, is $2.82 \times 10^{20}\,\mathrm{cm}^{-3}$ ($1.19 n_{crit}$). This higher electron density for LSFL is to be expected as a higher fluence was used (0.43 vs 0.36 J/cm^2) and a metallic surface is required for SPPs to be excited. The coupling of energy to the surface is stronger at these higher fluences, resulting in a $\sim 1\,\mu$m ripple depth as opposed to the $\sim$100 nm ripple depths observed here with HSFL.

Because the HSFL periods were measured by taking the FFT of the central region, it is worth noting that these electron densities should be taken as averages over the region in which central HSFL were observed to form. While the peak fluence was used in the calculation of the electron densities, using the average fluence of the central HSFL region changes the predicted value by $\sim$2%, so the former was used to simplify the calculations. In principle, the decrease in local fluence from the center outward results in a decrease in electron density and, therefore, a variation in the HSFL period. However, because the Kerr effect opposes the effect of Drude excitation, the HSFL period is less sensitive to changes in fluence than it would be otherwise, particularly for Ge with its large $\chi^{(3)}$. In addition to this, the central HSFL regions are relatively small with only modest variations in local fluence. For example, the decrease in fluence in Fig. 1(a) from the center of the damage spot to the outermost edge of the central HSFL region is less than 10%. As a result, the variations in the HSFL period within the central region are difficult to distinguish from the stochastic fluctuations inherent to LIPSS formation.

3. Influence of multiple pulses

As the periods of LSFL have been known to vary with pulse number,[22,39] it is worth considering the effect it may have on the HSFL results presented here. In a study by Bonse and Krüger,[39] a decrease in the observed period of SPP-induced LIPSS on Si was reported when the number of pulses was increased from 1 to 1000. This decrease was attributed to three distinct effects:

1. A larger number of pulses requires lower fluences for the formation of LIPSS (0.15 to 0.42 J/cm^2 reported for Si), which would otherwise be washed out by the central ablation crater. The electron densities are therefore lower, resulting in a reduction in the period.
2. With each pulse, the depths of the ripples increasing, modifying the SPP dispersion relation in such a way as to decrease the period.[22]
3. For large pulse numbers, Bonse *et al*. observed LSFL to form in an annular region near the boundary of the damage spot surrounding the central ablation crater. As a result, the local angle of incidence (and, therefore, the LIPSS period) can be affected.

Given the influence of electron density on the grating wavevector of the central HSFL, the first effect would certainly be expected to change the period when the fluence is varied. In Subsection IV B 2, however, the influence of electron excitation was considered across wavelengths for *constant* fluence. The electron densities reported in Section IV B 2 are therefore unaffected by the pulse number as far as the first effect is concerned. The second effect is only relevant for SPP-induced LIPSS while the LIPSS studied here are caused by SSWs. Finally, the third effect is not expected to influence the reported electron density estimates as they were based on HSFL present at the center of the damage spot, away from the border.

In order to confirm the above expectations experimentally, central HSFL were also generated at normal incidence at a wavelength of 2.4 μm using 10 pulses with peak fluences from 0.36 to 0.38 J/cm^2. Though the ripples were not as deep due to the smaller number of pulses ($\sim$10 nm vs. $\sim$100 nm for 100 pulses), the period was found to be 830 ± 50 nm, which corresponds well to that of the 100 pulse HSFL sites at the same angle of incidence, within experimental uncertainty.

C. Amorphous layer

Based on the amorphization observed in the TEM results, one might expect ultrafast melting, the non-thermal process where the rapid excitation of electrons causes the lattice to destabilize and melt in $\sim$100 fs,[40] to have occurred. However, such a process requires electron densities of $\sim 10^{22}$ cm^{-3} for Ge,[40] while the electron densities achieved here are only $\sim 10^{20}\,\mathrm{cm}^{-3}$. This suggests that the amorphization observed here cannot be attributed to ultrafast melting. Additionally, pump-probe reflectivity measurements performed by Bonse *et al*.[23] showed ultrafast melting of *p*-doped Ge using $\lambda = 800$ nm, 130 fs pulses, but without amorphization. In that experiment, sufficiently high electron densities could be reached because of the higher fluences used (no less than 0.51 J/cm^2), the greater initial carrier concentrations from p-doping ($\sim 4 \times 10^{17}\,\mathrm{cm}^{-3}$ vs. $\sim 1 \times 10^{14}\,\mathrm{cm}^{-3}$), and the accessibility of single-photon ionization. For the wavelengths studied here, at least two photons are needed to excite an electron across the bandgap (0.67 eV indirect, 0.81 eV direct). Additionally, the melting observed by Bonse *et al*. was due to single pulses as opposed to the many pulses used here. The amorphization observed in Fig. 1 must have therefore been caused by either multi-pulse effects or thermal melting from two-photon absorption (TPA).

For the parameters of Fig. 1, the electron density is found to be $2.41 \times 10^{20}\,\mathrm{cm}^{-3}$, which can be used to construct

a simple model to analyze the observed laser-induced amorphization. This was performed by modeling a laser pulse incident upon a semi-infinite slab of Ge with a refractive index given by the square root of Eq. (5) and an optical penetration depth given by $\delta_p = c/(2\omega \mathrm{Im}[n])$. The laser pulse was modeled as Gaussian in time (accounting for the change in the Kerr effect with intensity throughout the pulse) and the decay of the electric field strength was assumed to be due to absorption. The total energy absorbed as a function of depth was then determined. However, under the specified laser conditions, the energy absorbed never exceeded 0.2 eV/atom, well below the energy needed for the melting of 0.6 eV/atom (this includes the enthalpy of the fusion of 0.38 eV/atom for Ge). The thermal accumulation due to multiple pulses was also found to be negligible due to the large pulse separation (1 ms).[20] The formation of this amorphous layer therefore cannot be attributed to Fresnel absorption. Instead, it is necessary to consider two-photon absorption (TPA) according to the expression $\mathrm{d}I(z)/\mathrm{dz} = -\beta I^2$, where β is the TPA coefficient and I is the intensity. In order to obtain an accurate estimate of the energy absorbed due to this effect, a value of β at a 2.4 μm wavelength in the femtosecond regime with high intensities ($\sim$TW/cm^2) is needed, which is currently lacking. A rough estimate can be made by using the values of $\beta = 80$ cm/GW reported by Rauscher and Laenen.[41] for 2.9 μm light in the picosecond regime with intensities up to 2 GW/cm^2. Scaling to a 2.4 μm wavelength based on the photon energy yields $\beta = 66$ cm/GW. Using this value to determine the energy absorption as a function of depth suggests the formation of a melted layer extending down to 135 nm. However, the values of β have been known to decrease with pulse duration for SiO_2 (see Table I in Dragonmir *et al.*[42]). This would be expected to hold true for Ge as well when considering the band structure of Ge and the short-pulse, sub-bandgap photons under consideration here. For pulses $\gtrsim 1$ ps, multiple two-photon ionization pathways are available due to the accessibility of phonon-assisted transitions from the valence band to the conduction band. In the case of $\sim$100 fs pulses, however, electron-phonon collisions are too infrequent to allow for indirect transitions,[43] including the transition across the indirect bandgap of 0.67 eV. As a result, only the direct transition (0.81 eV) can occur. Additionally, with fewer ionization pathways available, state-filling[44] can occur, resulting in an increased effective bandgap. These combined effects would reduce the probability of TPA.

Another possible mechanism of amorphous layer formation is the formation of defect states after exposure to multiple laser pulses. While a disordered lattice configuration would be entropically favorable, the lower internal energy of an ordered lattice more than makes up for this difference in entropy when the crystal is below the melting temperature. With the introduction of defects, however, the internal energy of the crystalline phase can be increased until the material changes to an amorphous phase in order to lower its Gibbs free energy.[45] A better understanding of this process could be developed by studying how the depth of the amorphous layer changes as a function of the number of pulses.

D. Peripheral HSFL

The peripheral HSFL exhibit multiple properties that distinguish them from the central HSFL:

1. They form near the boundary of the damage spot.
2. Like the central HSFL, their direction is primarily parallel to the polarization. However, they exhibit a tendency to curve along the boundary.
3. Their period is very small, $\sim\lambda/8$ near the boundary.
4. Their period increases to $\sim\lambda/4$ further away from the boundary.
5. Their depth diminishes from the boundary inward, often leaving a LIPSS-free intermediate region before the central HSFL become visible.

Based on these properties, two models are proposed here to explain their formation. The first is simply diffraction off of the boundary of the damage spot, similar to the LIPSS of Murphy *et al.*[46] observed to form from the edges of gold microstructures. This would explain properties 1, 2, and 5 of the peripheral HSFL. However, such a model would also predict periods of $\sim\lambda/n$ for normal incidence, inconsistent with the peripheral HSFL observed in Fig. 1(b). From this model, it is not clear why the HSFL would have such short periods and why the period would increase further from the boundary.

The second model is based on the reflection of SSWs off of the boundary of the damage spot, followed by their interference with the incident light as well as the original SSW. This is depicted in Fig. 4 where a SSW with scattering angle ϕ reflects off of a particular point on the boundary (referred to as a reflecting plane). The location of this reflecting plane is defined by the angle ψ and can, in general, take on values ranging from 0 to 2π. For a given reflecting plane angle ψ, any scattering angles must satisfy $\psi - \pi/2 < \phi < \psi + \pi/2$ in order to be incident on the plane. With all possible interference combinations considered, there are five additional expressions analogous to Eq. (1)

$$\mathbf{k}_{\parallel} - \mathbf{k}_{sr} = \mathbf{G}, \tag{8a}$$

$$\mathbf{k}_{s} - \mathbf{k}_{sr} = \mathbf{G}, \tag{8b}$$

$$\mathbf{k}_{\parallel} - (\mathbf{k}_{s} + \mathbf{k}_{sr}) = \mathbf{G}, \tag{8c}$$

$$\mathbf{k}_{sr} - (\mathbf{k}_{s} + \mathbf{k}_{\parallel}) = \mathbf{G}, \tag{8d}$$

$$\mathbf{k}_{s} - (\mathbf{k}_{sr} + \mathbf{k}_{\parallel}) = \mathbf{G}, \tag{8e}$$

where $\mathbf{k}_{sr}$ is the wavevector of the reflected surface-scattered-wave (RSSW). Each of these expressions will yield a LIPSS period and orientation that varies as a function of both ψ and ϕ_r, the angle at which the SSW is incident upon the reflecting plane. These periods and grating vector angles were calculated for all possible combinations of ψ and ϕ_r for 45° angle of incidence. Eq. (8a) represents ordinary interference of the RSSW with the incident light. Eq. (8c) predicts a period that is unrealistically large ($\gtrsim\lambda$) for ϕ_r near normal incidence. Eqs. (8b), (8d), and (8e) all predict periods consistent with those observed for the peripheral HSFL at all values of ϕ_r that are not near grazing incidence. The

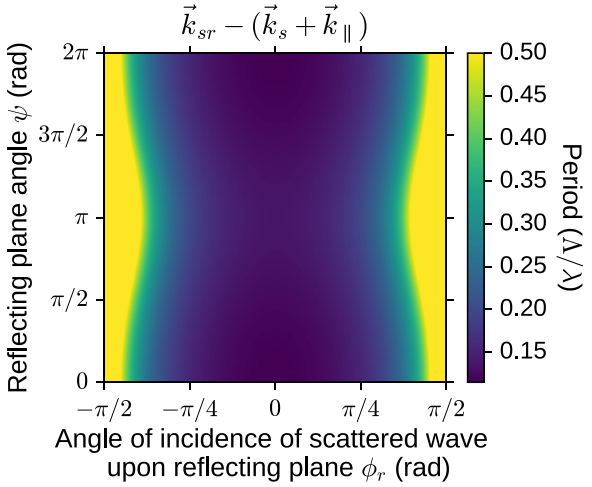

FIG. 8. LIPSS period (normalized to laser wavelength and contrast adjusted) as predicted by Eq. (8e) for 45° angle of incidence. This period is plotted as a function of reflecting plane angle ψ and the SSW's angle of incidence upon the reflecting plane ϕ_r. Except for values of ϕ_r near grazing incidence, all combinations of ψ and ϕ_r predict periods near the observed values for the peripheral HSFL. Very similar results are found for Eqs. (8b) and (8d).

solutions to Eq. (8d) are plotted in Fig. 8; the solutions to Eqs. (8b) and (8e) are omitted for brevity as they are qualitatively and quantitatively very similar to Eq. (8e). In this plot, the points where $\psi = 0$, π corresponds to the right and left sides of the damage spot in Fig. 9, respectively, and the points where $\psi = \pi/2$ corresponds to the top. These three equations also predict that the grating vector angle will be equal to ψ, i.e., the LIPSS will curve along the boundary of the damage spot. This model therefore predicts the formation of very high spatial frequency LIPSS ($\sim\lambda/8$) near the boundary of the damage spot with an orientation that curves along it. It is also feasible that the interference of two RSSWs could give rise to the HSFL observed at the sides of the damage spot. Finally, the lack of HSFL in the intermediate region could be a consequence of the time it takes the SSWs to propagate along the surface. For example, consider the most intense SSWs generated near the center of the damage spot in Fig. 1(b). These waves would propagate $\sim 10\,\mu$m

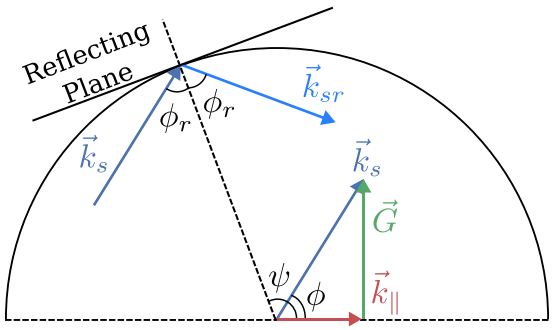

FIG. 9. Same diagram as Fig. 4 but with the reflection of a SSW from the boundary of the damage spot. The plane from which this reflection occurs is referred to as the reflecting plane. The position of this plane is described by the angle ψ, which can take on any value ranging from 0 to 2π. The angle at which the SSW is incident upon the reflecting plane is denoted by ϕ_r. The reflected surface-scattered-wave (RSSW) has wavevector $\mathbf{k}_{sr}$. The possible combinations of interference between the three wavevectors $\mathbf{k}_{\parallel}$, $\mathbf{k}_s$, and $\mathbf{k}_{sr}$ are described by Eq. (8).

before reflecting off of the boundary of the damage spot. The time it would take to travel this distance would be $\approx 10\,\mu$m/$(c/n) \approx 130$ fs. In other words, the incident laser pulse (FWHM duration of 90 fs) ends before the RSSW is able to reach the intermediate region and is therefore unable to interfere with it. This model would then be able to explain properties 1–3,5. However, it is not clear from this model why the period would increase further from the boundary. Further studies would be needed to determine if either of these models, with or without modification, can fully explain the observed properties of the peripheral HSFL.

V. CONCLUSION

In summary, the formation of HSFL in Ge using sub-bandgap, mid-IR, ultra-short laser pulses was systematically studied while varying multiple laser parameters including wavelength, angle of incidence, and polarization. The formation of the central HSFL is consistent with an SDK surface-scattered wave model of LIPSS formation. This is in contrast to the LSFL formation mechanism in the same wavelength regime[21] where higher fluences generate a metallic surface layer, allowing for the excitation of SPPs and their subsequent interference with the incident laser light. The inclusion of Drude excitation in the SDK model allows for an estimate of the electron density after laser-excitation. These estimates were significantly influenced by the Kerr effect because of the highest third-order susceptibility of Ge. With these effects taken into account, it was found that central HSFL on Ge seem to form optimally when the electron density is approximately half of the surface critical density. Additionally, a mechanism was proposed for the formation of HSFL near the boundary region of damage spots, which stipulates that SSWs reflect off of the sharp boundary. The subsequent interference between the incident light, the incoming SSW, and the RSSW seems to form the peripheral HSFL with spatial frequencies double that of central HSFL. Finally, two possible mechanisms were introduced to qualitatively explain the formation of the amorphous layer in the HSFL region. To identify the mechanism for quantitative agreement with observations, further studies at different pulse numbers as well as a measurement of the TPA coefficient for Ge in the mid-IR and femtosecond regimes at TW/cm^2 intensities are needed.

SUPPLEMENTARY MATERIAL

See supplementary material for a higher resolution image of the TEM cross section.

ACKNOWLEDGMENTS

This material is based upon the work supported by the Air Force Office of Scientific Research (AFOSR), USA under Award Nos. FA9550-12-1-0454, FA9550-12-1-0047, and FA9550-16-1-0069 as well as the Air Force Research Laboratory, USA Award No. FA-9451-14-1-0351. The DiMauro group acknowledges the support from MIR MURI Award No. FA9550-16-1-0013. C. I. Blaga acknowledges the support from AFOSR YIP, Award No. FA9550-15-1-0203. D.

Austin and E. Chowdhury acknowledge Vitaly Gruzdev for helpful discussion.

[1]H. M. van Driel, J. E. Sipe, and J. F. Young, Phys. Rev. Lett. **49**, 1955 (1982).
[2]A. Y. Vorobyev and C. Guo, Laser Photonics Rev. **7**, 385 (2013).
[3]J. E. Carey, C. H. Crouch, M. Shen, and E. Mazur, Opt. Lett. **30**, 1773 (2005).
[4]X. Liu, P. R. Coxon, M. Peters, B. Hoex, J. M. Cole, and D. J. Fray, Energy Environ. Sci. **7**, 3223 (2014).
[5]P. S. Goley and M. K. Hudait, Materials **7**, 2301 (2014).
[6]L. Tang, S. E. Kocabas, S. Latif, A. K. Okyay, D.-S. Ly-Gagnon, K. C. Saraswat, and D. A. B. Miller, Nat. Photonics **2**, 226 (2008).
[7]L. Zhang, A. M. Agarwal, L. C. Kimerling, and J. Michel, Nanophotonics **3**, 247 (2013).
[8]R. Soref, Nat. Photonics **4**, 495 (2010).
[9]F. K. Tittel, D. Richter, and A. Fried, "Mid-infrared laser applications in spectroscopy," in *Solid-State Mid-Infrared Laser Sources* (Springer, Berlin, Heidelberg, 2003), pp. 458–529.
[10]B. Jalali, Nat. Photonics **4**, 506 (2010).
[11]Y. Ishikawa and K. Wada, in *Sixth International Conference on Silicon Epitaxy and Heterostructures* [Thin Solid Films **518**, S83 (2010)].
[12]A. Boltasseva and H. A. Atwater, Science **331**, 290 (2011).
[13]M. A. Green, K. Emery, Y. Hishikawa, W. Warta, and E. D. Dunlop, Prog. Photovoltaics **23**, 1 (2015).
[14]S. Ghimire, A. D. DiChiara, E. Sistrunk, P. Agostini, L. F. DiMauro, and D. A. Reis, Nat. Phys. **7**, 138 (2011).
[15]H. Pires, M. Baudisch, D. Sanchez, M. Hemmer, and J. Biegert, Prog. Quantum Electron. **43**, 1 (2015).
[16]T. Popmintchev, M.-C. Chen, D. Popmintchev, P. Arpin, S. Brown, S. Ališauskas, G. Andriukaitis, T. Balčiunas, O. D. Mücke, A. Pugzlys, A. Baltuška, B. Shim, S. E. Schrauth, A. Gaeta, C. Hernández-García, L. Plaja, A. Becker, A. Jaron-Becker, M. M. Murnane, and H. C. Kapteyn, Science **336**, 1287 (2012).
[17]Q. Wu, Y. Ma, R. Fang, Y. Liao, Q. Yu, X. Chen, and K. Wang, Appl. Phys. Lett. **82**, 1703 (2003).
[18]J. E. Sipe, J. F. Young, J. S. Preston, and H. M. van Driel, Phys. Rev. B **27**, 1141 (1983).
[19]A. Borowiec and H. K. Haugen, Appl. Phys. Lett. **82**, 4462 (2003).
[20]R. Le Harzic, F. Stracke, and H. Zimmermann, J. Appl. Phys. **113**, 183503 (2013).
[21]D. R. Austin, K. R. P. Kafka, S. Trendafilov, G. Shvets, H. Li, A. Y. Yi, U. B. Szafruga, Z. Wang, Y. H. Lai, C. I. Blaga, L. F. DiMauro, and E. A. Chowdhury, Opt. Express **23**, 19522 (2015).
[22]M. Huang, F. Zhao, Y. Cheng, N. Xu, and Z. Xu, ACS Nano **3**, 4062 (2009).
[23]J. Bonse, G. Bachelier, J. Siegel, and J. Solis, Phys. Rev. B **74**, 134106 (2006).
[24]J. Byskov-Nielsen, J.-M. Savolainen, M. S. Christensen, and P. Balling, Appl. Phys. A **101**, 97 (2010).
[25]D. Dufft, A. Rosenfeld, S. K. Das, R. Grunwald, and J. Bonse, J. Appl. Phys. **105**, 034908 (2009).
[26]R. M. Langford and A. K. Petford-Long, J. Vac. Sci. Technol. A **19**, 2186 (2001).
[27]E. M. Hsu, T. H. R. Crawford, C. Maunders, G. A. Botton, and H. K. Haugen, Appl. Phys. Lett. **92**, 221112 (2008).
[28]M. Couillard, A. Borowiec, H. K. Haugen, J. S. Preston, E. M. Griswold, and G. A. Botton, J. Appl. Phys. **101**, 033519 (2007).
[29]M. Schade, O. Varlamova, J. Reif, H. Blumtritt, W. Erfurth, and H. S. Leipner, Anal. Bioanal. Chem. **396**, 1905 (2009).
[30]J. Reif, O. Varlamova, M. Ratzke, M. Schade, H. S. Leipner, and T. Arguirov, Appl. Phys. A **101**, 361 (2010).
[31]T. Tomita, T. Okada, H. Kawahara, R. Kumai, S. Matsuo, S. Hashimoto, M. Kawamoto, M. Yamaguchi, S. Ueno, E. Shindou, and A. Yoshida, Appl. Phys. A **100**, 113 (2010).
[32]S. Höhm, A. Rosenfeld, J. Krüger, and J. Bonse, J. Appl. Phys. **112**, 014901 (2012).
[33]S. Höhm, A. Rosenfeld, J. Krüger, and J. Bonse, Appl. Phys. Lett. **102**, 054102 (2013).
[34]J. F. Young, J. S. Preston, H. M. van Driel, and J. E. Sipe, Phys. Rev. B **27**, 1155 (1983).
[35]J. Bonse, M. Munz, and H. Sturm, J. Appl. Phys. **97**, 013538 (2005).
[36]M. Csete, O. Marti, and Z. Bor, Appl. Phys. A **73**, 521 (2014).
[37]R. D. Murphy, B. Torralva, D. P. Adams, and S. M. Yalisove, Appl. Phys. Lett. **103**, 141104 (2013).
[38]N. K. Hon, R. Soref, and B. Jalali, J. Appl. Phys. **110**, 011301 (2011).
[39]J. Bonse and J. Krüger, J. Appl. Phys. **108**, 034903 (2010).
[40]P. Stampfli and K. H. Bennemann, Phys. Rev. B **42**, 7163 (1990).
[41]C. Rauscher and R. Laenen, J. Appl. Phys. **81**, 2818 (1997).
[42]A. Dragonmir, J. G. McInerney, and D. N. Nikogosyan, Appl. Opt. **41**, 4365 (2002).
[43]V. G. Tyuterev, S. V. Obukhov, N. Vast, and J. Sjakste, Phys. Rev. B **84**, 035201 (2011).
[44]T. Numai, *Fundamentals of Semiconductor Lasers*, 2nd ed. (Springer, 2015).
[45]H. J. Fecht, Nature **356**, 133 (1992).
[46]R. D. Murphy, B. Torralva, D. P. Adams, and S. M. Yalisove, Appl. Phys. Lett. **102**, 211101 (2013).